Vibronic Coupling Effect on the Vibrationally-Resolved Electronic Spectra and Intersystem Crossing Rates of a TADF Emitter: 7-PhQAD

Sirong Lin,[†,¶] Zheng Pei,[†,¶] Bin Zhang,[†] Huili Ma,[*,‡] and WanZhen Liang[*,†]

†*State Key Laboratory of Physical Chemistry of Solid Surfaces, Fujian Provincial Key Laboratory of Theoretical and Computational Chemistry, and Department of Chemistry, College of Chemistry and Chemical Engineering, Xiamen University, Xiamen, Fujian 361005, P. R. China*

‡*Key Laboratory of Flexible Electronics & Institute of Advanced Materials, Nanjing University of Technology, 30 South Puzhu Road, Nanjing 211816, P. R. China*

¶*Contributed equally to this work*

E-mail: iamhlma@njtech.edu.cn; liangwz@xmu.edu.cn

Abstract

Assessing and improving the performance of organic light-emitting diode (OLED) materials require quantitative prediction of rate coefficients for the intersystem crossing (ISC) and reverse ISC (RISC) processes, which are determined not only by the energy gap and the direct spin-orbit coupling (SOC) between the first singlet and triplet excited states at a thermal equilibrium position of the initial electronic state but also by the non-Condon effects such as the Herzberg-Teller-like vibronic coupling

(HTVC) and the spin-vibronic coupling (SVC). Here we apply the time-dependent correlation function approaches to quantitatively calculate the vibrationally-resolved absorption and fluorescence spectra and ISC/RISC rates of a newly synthesized multiple-resonance-type (MR-type) thermally activated delayed fluorescence (TADF) emitter, 7-phenylquinolino[3,2,1-de]acridine-5,9-dione (7-PhQAD), with the inclusion of the Franck-Condon (FC), HTVC, and Duschinsky rotation (DR) effects. The SVC effect on the rates has also been approximately evaluated. We find that the experimentally-measured ISC rates of 7-PhQAD originate predominantly from the vibronic coupling, consistent with the previous reports on other MR-type TADF emitters. The SVC effect on ISC rates is about ten times larger than HTVC effect, and the latter increases the ISC rates by more than one order of magnitude while it slightly affects the vibrationally resolved absorption and fluorescence spectra. The discrepancy between the theoretical and experimental results is attributed to the inaccurate description of excited states calculated by the time-dependent density functional theory as well as not fully accounting for the complex experimental conditions. This work provides a demonstration of what proportion of ISC and RISC rate coefficients of a MR-type TADF emitter can be covered by the HTVC effect, and opens design routes that go beyond the FC approximation for the future development of high-performance OLED devices.

1 Introduction

The organic light-emitting diode (OLED) materials, based on fluorescence or phosphorescence emitters, have been successfully applied in displays and lighting.[1–5] The quantum yield of OLED devices, however, is usually low due to the limitation of spin statistics of electric current-generated excited-states and the exciton deactivations at high current density.[6,7] To take advantage of all the singlet and triplet excitons and then achieve 100% internal quantum efficiency (IQE), two strategies have been proposed based on "singlet-trapping" and "triplet-trapping", respectively.[8] The first one attempts to convert the singlet excitons

to triplet excitons through efficient intersystem crossing (ISC) induced by strong spin-orbit coupling (SOC) and therefore, obtains phosphorescence materials that emit light from the lowest triplet excited-state. The second strategy tries to achieve "delayed" fluorescence by converting triplet excitons to singlet excitons through reverse ISC (RISC) process with the help of thermal activation. In this regard, the performance of OLED device is inseparable from the ISC and RISC processes. Therefore, it is of particular importance for us to study the mechanism and quantitatively predict the rate coefficients.

It is apparent that the ISC and RISC processes are facilitated by negligible energy gap (ΔE_{ST}) and large SOC matrix element (SOCME) between the first singlet and triplet excited-states. These two conditions are usually rather controversial. However, in recent few years, the sufficiently fast RISC processes have been found in many systems with the sizable ΔE_{ST} and vanishingly small SOCME.[5,9] For these systems, their RISC mechanism has not been well understood. That's for sure that the high-order factors like the vibronic coupling should play a crucial role on their ISC/RISC processes. Unveiling the mechanism underlying that fast RISC process presents a challenge. Powerful computing resources and effective algorithms provide a way to resolve this challenge.[10–13]

Like the calculations of molecular vibronic spectra, the rate calculations with the inclusion of vibronic coupling effect require us to account for simultaneous changes in the vibrational and electronic states. One thus has to combine both the electronic structure theories and quantum dynamics methods to obtain the structure parameters and to describe the nuclear dynamics, respectively. The earliest research examples to characterize the vibronic properties were to calculate the phosphorescence of small aromatic hydrocarbons such as benzene.[14–16] Later, the vibronic effects were involved in the calculations of ISC rates of some small organic molecules,[17–20] and were demonstrated to be significant for the RISC rates of some TADF materials.[21–26]

One of the vibronic effects is captured by spin-vibronic coupling (SVC), represented by the third and fourth terms in RHS of Eq. (7), which require to calculate the other,

intermediate excited-states and nonadiabatic coupling (NAC) elements between the excited states. The NACs between the low-lying singlet and triplet excited-states open the possibility for significant second-order coupling effects. Many previous theoretical works have found that the second-order SVC could assist the triplet-to-singlet up-conversion and increase RISC rates by a few orders of magnitude in some TADF emitters.[21,25–29] Therefore, a full second-order SVC model was adopted to calculate S–T crossing rates (e.g. Refs 25–29). Usually, the second-order vibronic coupling effect in most cases is much smaller than the first-order one. However, due to a vibronic resonance that orchestrates the low-lying electronic states (S_1, T_1, T_2) together, S_1–T_n crossings may play a major role in enhancing ISC and RISC, especially for some MR-type TDAF emitters.[25,29,30]

Except the SVC, there is another vibronic coupling effect known as Herzberg-Teller-type vibronic coupling (HTVC).[31] This effect has been recognized and incorporated in the simulation of molecular vibronic specra.[32–41] Along this line, we have developed the time-dependent correlation function approach to account for the sumultaneous changes in the vibrational and electronic states[41] and calculated the electronic absorption and emission spectra and resonant Raman scattering spectra,[38,40] including the Franck-Condon (FC), HTVC, and Duschinsky rotation (DR)[42,43] effects. This method could be naturally extended to calculate the ISC and RISC rates. It should be interesting to see what proportion of its ISC/RISC rate can be covered by the HTVC effect for a MR-type emitter. We aim to provide a demonstration in this work.

Recently, Li et al[44] synthesized a narrow-band, ultrapure blue TADF material, 7-PhQAD (shown in Fig. 1), which is based on a rigid framework of quinolino-[3,2,1-*de*]acridine-5,9-dione. Its S_1 and T_1 states mainly possess (π, π^*) transition character so that the $S_1 \rightarrow T_1$ crossing is nearly spin-forbidden according to the El-Sayed's rule.[45] Furthermore, the experimentally measured S_1–T_1 energy gap of $\Delta E_{\mathrm{ST}} = 1532$ cm^{-1} (0.19 eV), which is quite large. Nevertheless, the experimental ISC and RISC rates actually reach 1.5×10^8 and 6.4×10^3 s^{-1}, respectively, which indicates the significant impact of the vibronic coupling effects. Here we

calculate the vibrationally resolved absorption and fluorescence spectra as well as its ISC and RISC rates with HTVC effect to verify the microscopic mechanism of TADF process. We aim to describe its photophysical properties, quantitatively predict the ISC and RISC rates, and unveil the behind mechanisms. The time-dependent correlation function approaches will be adopted.

2 Theoretical Methods

With respect to the Fermi-Golden rule,[46] the transition rate (k) from the initial state i to a dense manifold of final states f can be described as

$$k_i = \frac{2\pi}{\hbar} \sum_f \mid \langle \Phi_f \mid \hat{H}' \mid \Phi_i \rangle \mid^2 \delta(\hbar\omega - (E_f - E_i)), \tag{1}$$

where $|\Phi_i\rangle$ and $|\Phi_f\rangle$ are the wavefunctions of the initial and final vibronic states, respectively, ω is the frequency of the external radiation. $\hat{H}'$ denotes the perturbation and can be written as $\hat{H}' = -\vec{\mu} \cdot \vec{f} + \hat{T}_{\mathrm{N}} + \hat{H}_{\mathrm{SO}}$, where the first, second and third operators correspond to the matter-field interaction, the nuclear kinetic energy, and spin-orbit interaction, respectively. The radiative transition like electronic absorption or emission is usually governed by the matrix element of $\langle \Phi_f \mid \hat{\mu} \mid \Phi_i \rangle$ while the nonradiative processes like internal conversions and ISCs or RISCs are determined by the matrix elements of latter two operators. If we introduce the integral representation of the delta function $\delta(\hbar\omega - (E_f - E_i)) = \frac{1}{2\pi} \int_{-\infty}^{+\infty} e^{i(\omega - \frac{E_f - E_i}{\hbar})t} dt$, and define $\hat{H}'(t) = e^{-\frac{i\hat{H}t}{\hbar}} \hat{H}' e^{\frac{i\hat{H}t}{\hbar}}$, the rate equation becomes

$$\begin{aligned} k_i &= \frac{1}{\hbar} \int_{-\infty}^{+\infty} \sum_f \langle \Phi_f \mid \hat{H}'(t) \mid \Phi_i \rangle \cdot \langle \Phi_i \mid \hat{H}' \mid \Phi_f \rangle e^{\omega t} dt \\ &= \frac{1}{\hbar} \int_{-\infty}^{+\infty} \langle \Phi_i \mid \hat{H}' \cdot \hat{H}'(t) \mid \Phi_i \rangle e^{i\omega t} dt. \end{aligned} \tag{2}$$

For ISC process, if we restrict ourselves up to second-order terms, the coupling matrix

element can be expressed as[16,47]

$$\begin{aligned} H'_{fi} &= \langle {}^3\Phi_f \mid \hat{H}_{\rm SO} \mid {}^1\Phi_i \rangle \\ &+ \sum_{m \neq i} [\langle {}^3\Phi_f \mid \hat{H}_{\rm SO} \mid {}^1\Phi_m \rangle \langle {}^1\Phi_m \mid \hat{T}_{\rm N} \mid {}^1\Phi_i \rangle / (E_i - E_m)] \\ &+ \sum_{n \neq f} [\langle {}^3\Phi_f \mid \hat{T}_{\rm N} \mid {}^3\Phi_n \rangle \langle {}^3\Phi_n \mid \hat{H}_{\rm SO} \mid {}^1\Phi_i \rangle / (E_f - E_n)], \end{aligned} \tag{3}$$

where the summations extend over the complete sets of pure-spin Born-Oppenheimer (psBO) states of the given multiplicity. The first term is called as the direct SOCME, and the last two terms originate from the mixed vibronic and SOC, usually called as the SVC. Although Eq. (3) specifically refers to a S→T crossing, the corresponding expression for the reverse crossing is readily written down. Taken the three components ($m_s = 0, \pm 1$) of a triplet state into account, the root-mean-square SOCMEs

$$\langle {}^1\Psi_n \mid \hat{H}_{\rm SO} \mid^3 \Psi_m \rangle = \sqrt{\sum_{m_s=0,\pm 1} \parallel \langle {}^1\Psi_n \mid \hat{H}_{\rm SO} \mid^3 \Psi_m^{m_s} \rangle \parallel^2} \tag{4}$$

are used in above evaluations of SOC between ${}^1\Psi_n$ and ${}^3\Psi_m$ states.

One may evaluate Eq. (3) by making use of the HT expansion, i.e., expand the integrals about the nuclear equilibrium configuration $Q = 0$. Writing the psBO functions as products of an electronic wavefunction Ψ and a vibrational wavefunction Λ like ${}^\sigma\Phi_n(q,Q) = {}^\sigma\Psi_n(q,Q)\Lambda_n(Q)$, we have

$$ {}^\sigma\Psi_n(q,Q) = {}^\sigma\Psi_n(q,0) + [\partial {}^\sigma\Psi_n(q,0)/\partial Q]_{Q=0}\, Q + \cdots , \tag{5}$$

$$ H^{if}_{\rm SO} = H^{if}_{\rm SO} \mid_{Q=0} + \left[\partial H^{if}_{\rm SO}/\partial Q\right]_{Q=0} Q + \cdots . \tag{6}$$

The second term in Eq. (6) originates from vibronically induced SOC or the HT-like expansion. If we terminate the expansions after the lowest-order nonvanishing term, H'_{if} in Eq.

(3) can be written as[16,47]

$$H'_{fi} = H_{SO}^{fi} \mid_{Q=0} \langle \Lambda_f(Q') | \Lambda_i(Q) \rangle + \sum_{k=1}^{3N-6} \left(\frac{\partial H_{SO}^{fi}}{\partial Q_k} \mid_{Q=0} \langle \Lambda_f(Q') | Q_k | \Lambda_i(Q) \rangle \right) - \sum_{k=1}^{3N-6} \left(\left[\sum_{m \neq i} \frac{H_{SO}^{fm} H_{mi,1}^{k}}{(E_i - E_m)} + \sum_{n \neq f} \frac{H_{fn,3}^{k} H_{SO}^{ni}}{(E_f - E_n)} \right]_{Q=0} \langle \Lambda_f(Q') | \frac{\partial}{\partial Q_k} | \Lambda_i(Q) \rangle \right), \quad (7)$$

where the relation of

$$\langle {}^{\sigma}\Phi_e \mid \hat{T}_{\mathrm{N}} \mid {}^{\sigma}\Phi_r \rangle \sim - \sum_{k=1}^{3N-6} \langle {}^{\sigma}\Psi_e \mid \nabla_k \mid {}^{\sigma}\Psi_r \rangle \langle \Lambda_e(Q') | \nabla_k \Lambda_r(Q) \rangle \quad (8)$$

is applied, then we define

$$H_{er,\sigma}^{k} = \langle {}^{\sigma}\Psi_e \mid \partial / \partial Q_k {}^{\sigma}\Psi_r \rangle \quad (9)$$

as the NAC vector between two excited states of the given spin multiplicity σ. It is noted that the second derivatives of Ψ_r or Λ_r with respet to the nuclei coordinates have been neglected. If the first term, the direct SOC, vanishes, this intersystem crossing is spin forbidden. The second term denotes to the nuclear derivatives of a given SOCME between initial and final states with different spin. And if it gets involved in the rate calculations, we refer its contribution as the HTVC effect in this article.

If the harmonic oscillator approximation to the potential energy surfaces is adopted, then the calculations of S–T crossing rates are similar to the calculation of vibrationally-resolved absorption and fluorescence spectra. In the latter cases, SOC operator is replaced with the dipole operator $\hat{\mu}$, and S_0 and S_1 states are concerned. We have implemented these time-dependent correlation function approaches to calculate the vibronic spectra including one- and two-photon absorption and emission[39,40] and resonance Raman scattering spectra.[38] A summary of our previous works on the vibronic spectra has been given in Ref. 41. Here we extend this time-dependent approach to calculate the S–T crossing rates.

Within the adiabatic approximation the molecular Hamiltonian can be written as $\hat{H} =|$

$\Psi_i\rangle\hat{H}_i\langle\Psi_i \mid + \mid \Psi_f\rangle(\hat{H}_f + \Delta E)\langle\Psi_f \mid$, where $\hat{H}_i$ and $\hat{H}_f$ represent the vibrational Hamiltonians of the initial and final vibronic states, respectively. If we account for the Boltzmann distribution of the initial-state vibronic manifold at the finite temperature and the molecular energy conservation for the nonradiative transition, i.e. $\omega = 0$, Eq. (2) becomes the following thermal rate constant form for the transition from the initial to the finial electronic states

$$k(T) = \frac{1}{\hbar}\int_{-\infty}^{+\infty} dt e^{(-i\Delta Et/\hbar + i\gamma t - \gamma t^2/\beta)} C(t), \tag{10}$$

with $C(t) = \frac{Tr[e^{-\beta\hat{H}_i}\hat{H}' e^{-i\hat{H}_f t/\hbar}\hat{H}' e^{iH_i t/\hbar}]}{Tr[e^{-\beta\hat{H}_i}]}$. Here $\beta = 1/k_{\mathrm{B}}T$, $Tr(\cdots)$ represents the trace over nuclear degrees of freedom, and $\hat{H}'$ denotes the coupling between the initial and final states, defined as $\hat{H}' = |\Lambda_i\rangle\overline{H}'_{if}\Lambda_f| + |\Lambda_f\rangle\overline{H}'_{fi}\langle\Lambda_i|$, where $\overline{H}'_{fi}$ includes the direct SOCME between the initial and final electronic states, its derivative terms, and the terms concerned with the products of NACs and SOCMEs,

$$\begin{aligned}\overline{H}'_{fi} = \quad & H_{SO}^{fi} \mid_{Q=0} + \sum_{k=1}^{3N-6}\left[\frac{\partial H_{SO}^{fi}}{\partial Q_k}\right]_{Q=0} Q_k \\ & - \sum_{k=1}^{3N-6}\left[\sum_{m\neq i}\frac{H_{SO}^{fm}H_{mi,1}^{k}}{(E_i - E_m)} + \sum_{n\neq f}\frac{H_{fn,3}^{k}H_{SO}^{ni}}{(E_f - E_n)}\right]_{Q=0}\frac{\partial}{\partial Q_k}.\end{aligned} \tag{11}$$

ΔE is the energy difference between two concerned electronic states of $|\Psi_i\rangle$ and $|\Psi_f\rangle$ (0-0 transition).

With respect to Eq. (11), the rate k can also be separated into FC-, HTVC- and SVC-related components. In our quantitative calculations of S–T crossing rates of 7-PhQAD, we only keep the first two terms of Eq. (11) and ignore the last two second-order spin-vibronic interactions. However, the contribution of SVC to the rates is roughly evaluated in Section 4.4 and Section S3 in the supporting information (SI).

γ represents the solvent reorganization energy, and the corresponding exponential function form of γ comes from the high temperature approximation of solvent mode.[48,49] The analytical expressions for the FC- and HT-like components in the rates, and the detailed

derivation of the exponential expression of γ has been given in section S1 and S2 of SI.

3 Computational Details

TADF emerges from a balance of charge-transfer (CT) and local excited states,[50–54] however, it is well-known that the conventional approximated exchange-correlation (XC) functionals and kernels can lead to a large error in TDDFT calculations of a TADF emitter. The tuned range-separated XC functionals have thus been suggested to describe the excited-states properties with inclusion of CT character.[55–59] Here, the conventional hybrid XC functional B3LYP,[60] and three optimally tuned range-separated XC functionals CAM-B3LYP*,[61] ω*B97X-D,[62,63] and LC-BLYP*[62,64] have been adopted. The parameter ω in these range-separated functionals are tuned by minimizing the function of $\sum_{i=0}^{i=1}[\varepsilon_{\mathrm{HOMO}}(\omega, N+i) + \mathrm{IP}(\omega, N+i)]^2$,[65,66] where $\varepsilon_{\mathrm{HOMO}}$ is the energy of the highest occupied molecular orbital (HOMO) and IP is the ionization energy.

All the calculations are carried out including the polarizable continuum model with the integral equation formalism variant[67–69] to mimic the toluene environment in experiments within Q-Chem 5.2 software package.[70] The full time-dependent density functional theory (TDDFT) and its Tamm-Dancoff approximation (TDA)[71] as well as 2th order algebraic diagrammatic construction (ADC(2))[72] are adopted to evaluate the singlet and triplet excited-states. In addition, 6-311++G** basis set is used for all the (TD)DFT calculations while a correlation consistent basis set, cc-pVDZ, is chosen for the ADC(2) method. The optimal structures of ground- and excited-states of 7-PhQAD molecule are optimized by DFT and TDA methods with CAM-B3LYP* functional, respectively. The Multiwfn3.7 package[73,74] is adopted to plot the MOs involved in the corresponding electronic excitations and the charge density differences between the corresponding excited states and ground state.

The derivatives of the SOCMEs with respect to the nuclear coordinates have been calculated numerically using a three-point finite-difference approximation with a step length of

0.001 Å. Considering the three degenerate electronic substates of the triplet ($m_s = 0, \pm 1$), the calculated RISC rate is scaled by a factor of 1/3. Moreover, the reported NAC values are calculated by taking norms of NAC vectors at three directions for individual atoms and then summing them up.

4 Results and Discussion

4.1 The Geometries and Electronic Structures

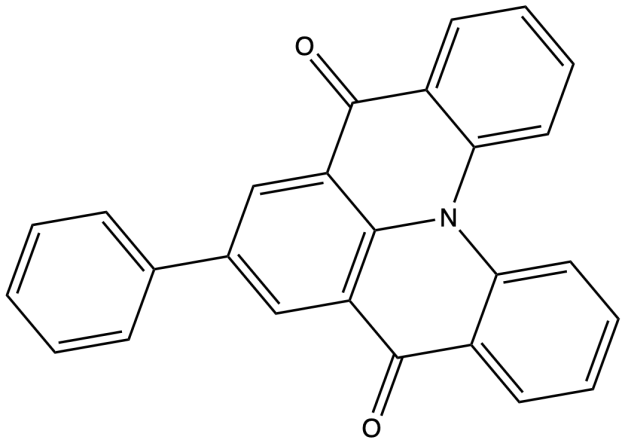

Figure 1: The chemical structure of 7-PhQAD molecule.

The geometry of 7-PhQAD molecule is shown in Fig. 1. The experimentally measured absorption and fluorescence maxima of 7-PhQAD in toluene are 446 nm (2.78 eV) and 464 nm (2.67 eV), respectively, with a Stokes shift of 18 nm.[44] The calculated vertical and adiabatic excitation energies (VEEs and AEEs) by TDA, full TDDFT, and ADC(2) methods are shown in Table 1. It is clear that TDDFT with and without TDA slightly overestimates the absorption and emission energies, and significantly overestimate the energy gap of $\Delta E_{\mathrm{S_1T_1}}$ compared to the experimental values of 1532 cm^{-1} (0.19 eV).[44] More specifically, the first three functionals (B3LYP, CAM-B3LYP*, and ωB97XD*) in Table 1 produce the vertical and adiabatic energy gaps $\Delta E_{\mathrm{S_1T_1}} \geq 0.5$ eV. The CAM-B3LYP* TDDFT calculations, for instance, predict vertical excitation energy of 2.87 and 2.36 eV for S_1 and T_1 states, respec-

tively. While the LC-BLYP* yields a slightly smaller $\Delta E_{S_1T_1}$ value of ~ 0.4 eV for vertical excitation and 0.3 eV for adiabatic transition.

Table 1: Vertical excitation energies (VEEs) and adiabatic excitation energies (AEEs) in a unit of eV on CAM-B3LYP* optimized geometries, calculated by TDA and TDDFT with four XC functionals and ADC(2) methods, respectively. The oscillator strengths are shown in parenthesis.

	States	B3LYP		CAM-B3LYP* $\omega = 0.071$		ωB97XD* $\omega = 0.032$		LC-BLYP* $\omega = 0.065$		ADC(2)
		TDA	TDDFT	TDA	TDDFT	TDA	TDDFT	TDA	TDDFT	
VEEs	T_1	2.40	2.36	2.40	2.36	2.51	2.47	2.07	2.06	2.92
	S_1	2.94	2.86	2.96	2.87	3.06	2.98	2.54	2.46	3.19
		(0.25)	(0.20)	(0.26)	(0.20)	(0.27)	(0.22)	(0.20)	(0.15)	(0.1715)
	T_2	3.07	2.95	3.07	2.95	3.16	3.03	2.49	2.48	3.14
	T_3	3.09	3.04	3.10	3.04	3.18	3.13	2.67	2.65	3.25
	S_2	3.38	3.37	3.39	3.38	3.47	3.46	2.70	2.69	3.36
		(0.00)	(0.0001)	(0.00)	(0.00)	(0.00)	(0.00)	(0.0024)	(0.0005)	(0.0003)
AEEs	T_1	2.30	2.26	2.31	2.21	2.41	2.37	1.99	1.98	
	T_2	2.87	2.79	2.87	2.72	2.96	2.85	2.30	2.28	
	S_1	2.86	2.78	2.88	2.73	2.98	2.89	2.46	2.38	3.04

The appreciable overestimation to $\Delta E_{S_1T_1}$ by the TDDFT approach indicates that 7-PhQAD molecule is a strongly correlated system. To check this, we calculate VEEs of low-lying excited states at the theoretical level of ADC(2)/cc-pVDZ. The ADC methods involve a perturbative expansion of a propagator followed by truncation at a certain order n that defines the ADC(n) approximation.[72] As concluded by previous studies on the MR-type TADF materials, the coupled-cluster (CC) family such as CC2 and CCSD or ADC approach such as ADC(2) could take double excitations or second-order dynamic electron correlation effect into account and therefore, reproduce more accurate S_1–T_1 energy gap than TDDFT does.[29,75,76] Even though ADC(2)/cc-pVDZ overestimates the absorption and emission energies (see Table S1 in SI), it produces a S_1–T_1 energy gap of 0.27 eV, which is much closer to the experimental measured value 0.19 eV. The second-order correction contributes 13% and 11% to S_1 and T_1 states, respectively, as Table S1 in SI shows, meaning

that the failure of TDDFT approach is owing to the absence of an explicit account of double (or higher order) excitations. To exactly describe 7-PhQAD molecule, one thus has to properly account for electron correlation.

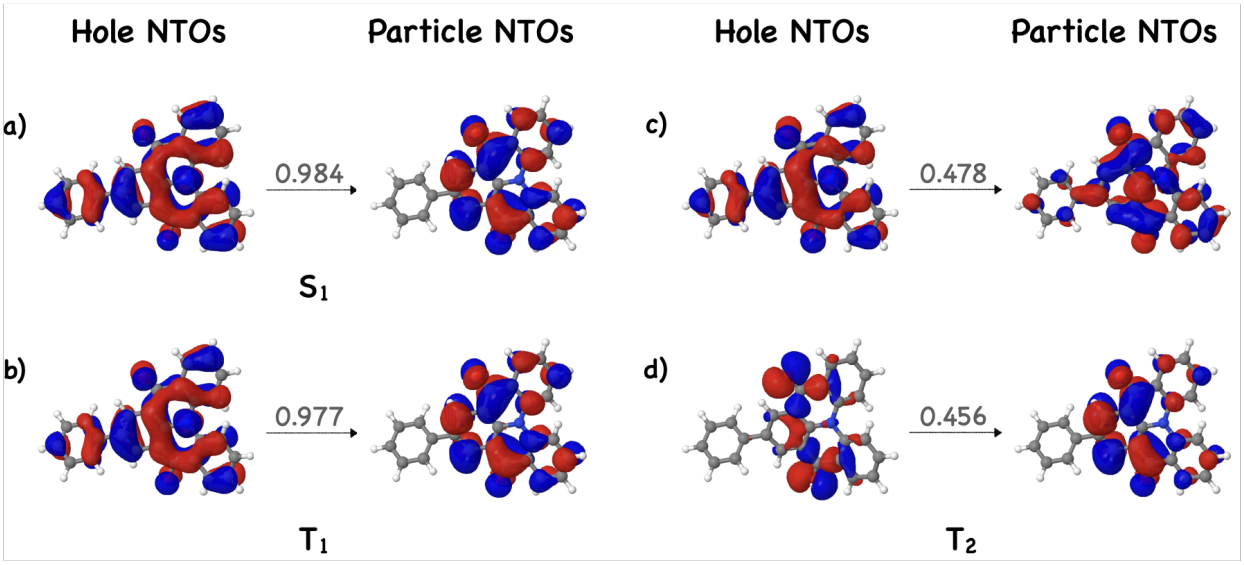

Figure 2: Natural transition orbitals (NTOs) of the S_1, T_1, and T_2 states of 7-PhQAD calculated by TDDFT method with CAM-B3LYP* ($\omega = 0.071$) functional and 6-311++G** basis set. Isovalue of 0.02 au is used.

For analyzing the excited states, the NTOs of three lowest excited-states at 7-PhQAD ground-state minimum are calculated. Fig. 2 exhibits the hole and particle NTOs of S_1, T_1, and T_2 states with largest contributions (coefficients larger than 0.1) to the corresponding excitations. The S_1 and T_1 states both are dominated by HOMO→LUMO transitions with a percentage of 95.1 and 96.1, respectively. Therefore, as illustrated by panels (a) and (b) in Fig. 2, the first pair of NTOs of S_1 and T_1 states are nearly identical, having the similar shapes as HOMO and LUMO shown in Fig. S3 of SI. These excitations are clearly (π, π^*) transitions with substantial intramolecular CT character, which is confirmed by the corresponding relaxed difference density plots shown in Fig. S4 of SI. Since the S_1 and T_1 states have similar hole and particle orbitals, the SOCME between these two states is deduced to be small, which is actually verified by the calculated values shown in Table 2.

Unlike S_0→S_1 and S_0→T_1 excitations, more pairs of MO transitions got involved in T_2

and T_3 states. For $S_0 \rightarrow T_2$ excitation, HOMO-3→LUMO and HOMO-4→LUMO+1 contribute 74.0% and 11.3%, respectively. Consequently, T_2 state has the partial character of (n, π^*) referring the MO plots in Fig. S3 of SI. Two pairs of NTOs contribute near equally to T_2 excitation, depicted in Fig. 2 as panels (c) and (d). For $S_0 \rightarrow T_3$, on the other hand, HOMO→LUMO+1 makes a major contribution, accounted for 55.1%, followed by HOMO-4→LUMO of 14.8%. As shown in panels (c) and (d) of Fig. S4 in SI, the relaxed density difference plots of T_2–S_0 and T_3–S_0 have local excitation character, which are different from those of S_1–S_0 and T_1–S_0. As a result, the SOCMEs between S_1 and T_2 and between S_1 and T_3 should be larger than that between S_1 and T_1, verified by the calculated values shown in Table 2.

According to the El-Sayed's rule, in order to compensate for the momentum change caused by electron spin reversal, it is necessary for an electron to jump in a mutually perpendicular orbit to balance the momentum change. Therefore, the initial and final states must have different transition properties to make ISC take place. But unfortunately, both S_1 and T_1 states of 7-PhQAD mainly have (π, π^*) character, indicating that the ISC and RISC between S_1 and T_1 state are nearly forbidden if only direct SOC is taken into account. The T_2 and T_3 are almost degenerate and close to S_1 in terms of energy (Table 1), along with the large SOCs of S_1–T_2 and S_1–T_3, suggesting that the population transition via $S_1 - T_n$ (n=2,3) may potentially play a crucial role in S–T crossings.

Considering the intramolecular CT and (π, π^*) characters of the excited states, we use the optimally-tuned XC functional CAM-B3LYP* in the following spectral and rates' calculations.

4.2 Vibrationally-Resolved Absorption and Fluorescence Spectra

The calculated vibrationally resolved absorption and fluorescence spectra are shown in Fig. 3. In our calculations, the adiabatic energy gap between S_0 and S_1 states (0-0 transition) is set to be nearly same with the calculated value by TDA-CAM-B3LYP*. The theoretical

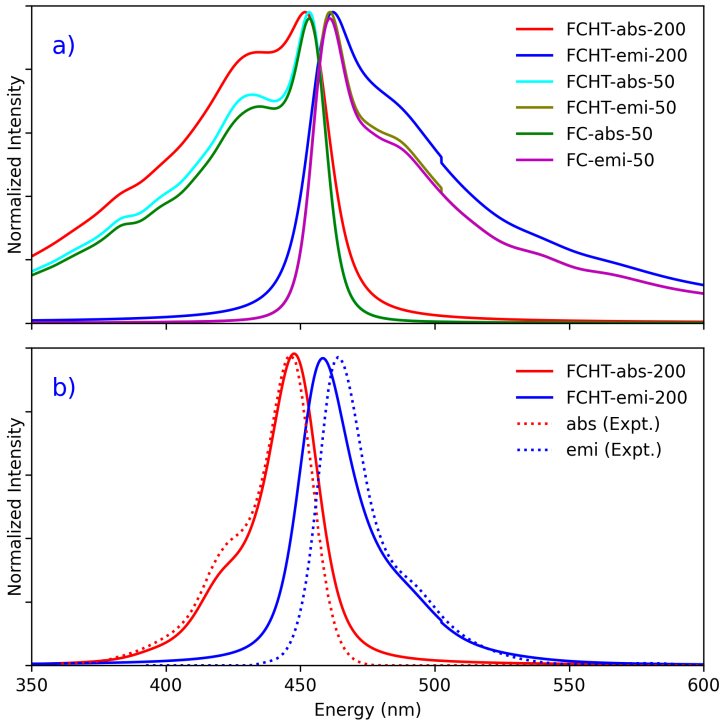

Figure 3: The calculated vibrationally resolved absorption (left) and fluorescence (right) spectra at $T = 300.0$ K with different approximations. The top panel: FC and FCHT approximations with inclusion of DR effect at the damping factor $\gamma = 200$ and 50 cm^{-1}, respectively. The bottom panel: FCHT result with VG approximation at $\gamma = 200$ cm^{-1}. For better comparison, the calculated spectra are red-shifted by 6.0 and 15 nm for the results without and with VG approximation, respectively.

calculation with the vertical gradient (VG) approximation[40,43,77] produces a narrow-band absorption and emission with very small full-width at half-maximum (FWHM), which coincides with the experimental measurements. The spectral lineshapes indicate that this material possesses a rigid nature which can significantly reduce the vibrational motion to obtain narrow-band emission with very small FWHM. The VG approximation assumes that the S_1 potential energy surface (PES) is just a shifted PES of the S_0, meaning that the electronic excitation doesn't change the shape of PES much. The theoretical calculation without VG approximation accounts for the difference between S_0 and S_1 PESs, and largely overestimates FWHM compared to the experimental value, attributed to the inaccurate S_1 PES calculated by the TDDFT method. The HTVC effect on the absorption and emission

spectra is negligibly small.

As demonstrated by the key geometrical parameters listed in Table S3 of SI, TDDFT with and without TDA predicts a larger difference between the ground-state and S_1 excited-state geometries than ADC(2) does because TDDFT produces a more twisted conformation for S_1 state. Furthermore, 7-PhQAD adapts similar geometry under different types of electronic excitations from $S_0 \rightarrow S_1$ and $S_0 \rightarrow T_1$. As shown in Table S2 of SI, the optimized geometrical structures of S_1 and T_1 only exhibit a slight difference in the dihedral angles, for instance, it is 26.6^o and 24.6^o between the benzene ring and the main body, respectively, from TDA-CAM-B3LYP* calculations. The root mean square deviation (RMSD) between S_1 and T_1 geometric parameters is only 0.02 Å (see Fig. S2 in SI). The minimal configuration change satisfies the condition of harmonic oscillator approximation, ensuring that the subsequent calculations of ISC and RISC rates are effective and reliable.

4.3 ISC and RISC Rates with inclusion of FC and HTVC effects

Table 2: The SOCMEs and norms of NAC vectors (NACs) with respect to the geometries of S_1 and T_1 states, respectively, calculated by TDA method with CAM-B3LYP* ($\omega = 0.071$) functional and 6-311++G** basis set.

Transitions	SOCME (cm^{-1})		Transitions	NACs (au)	
	S_1 Geom.	T_1 Geom.		S_1 Geom.	T_1 Geom.
T_1–S_1	0.14	0.15	T_1–T_2	19.50	18.65
T_2–S_1	3.78	4.68	T_1–T_3	7.79	5.69
T_3–S_1	8.92	10.15	T_2–T_3	85.44	214.51
T_1–S_2	13.04	14.30	S_1–S_2	10.61	9.09
T_1–S_3	4.82	3.71	S_1–S_3	19.41	21.09

Table 2 collects the calculated SOCMEs and the norms of NAC vectors of the lowest three singlet and triplet states at S_1 and T_1 geometries. As deduced from the NTOs and MOs of S_1 and T_1 states, the SOCMEs of S_1–T_1 are 0.14 and 0.15 cm^{-1} with respect to S_1 and T_1 geometries, respectively, which are relatively small. The experimentally measured ISC rate of S_1–T_1 transition is quite large, however, suggesting that the contribution of

vibronic coupling effects on the rates of S_1–T_1 crossings should be significant. Here we thus calculate both the ISC and RISC rates with the inclusion of the FC, HTVC, and DR effects. A result comparison is made with the VG approximation. In our rate calculations, the experimental energy gap 1532 cm^{-1} is used for S_1-T_1 transitions, whereas for S_1-T_2 crossings, we set $\Delta E_{S_1T_2} = 74$ cm^{-1} as the calculated adiabatic energy gap between S_1 and T_2 by TDA-CAM-B3LYP*.

Table 3: Calculated k_{ISC} and k_{RISC} (s^{-1}) of S_1–T_1 and S_1–T_2 transitions at different temperatures T (K) by FC and HT formulas with or without VG approximation, where γ is set to be 20 cm^{-1}. Experimental rates are also shown as comparisons.

Rates	T (K)	without VG approximation		with VG approximation				Expt.
				S_1 Geom.		T_1 Geom.		
		FC	HT	FC	HT	FC	HT	
$k_{S_1\to T_1}$	298	3.4×10^{7}	5.4×10^{8}	2.3×10^{7}	4.8×10^{8}	1.8×10^{7}	5.7×10^{8}	1.5×10^{8}
	100	2.6×10^{7}	4.5×10^{8}	1.9×10^{7}	4.1×10^{8}	1.4×10^{7}	5.2×10^{8}	
	50	2.4×10^{7}	4.4×10^{8}	1.6×10^{7}	3.5×10^{8}	1.1×10^{7}	3.6×10^{8}	
$k_{S_1\to T_2}$	298	8.0×10^{9}		3.5×10^{11}		7.8×10^{10}		
	100	7.5×10^{9}		4.8×10^{11}		1.2×10^{11}		
	50	2.1×10^{9}		4.1×10^{11}		1.3×10^{11}		
$k_{T_1\to S_1}$	500	3.1×10^{5}	3.3×10^{5}	1.3×10^{5}	2.9×10^{5}	1.1×10^{5}	2.5×10^{5}	
	400	1.1×10^{5}	2.8×10^{5}	4.4×10^{4}	2.8×10^{5}	3.5×10^{4}	2.6×10^{5}	
	350	5.3×10^{4}	2.8×10^{5}	2.0×10^{4}	2.8×10^{5}	1.6×10^{4}	2.6×10^{5}	
	298	1.9×10^{4}	2.8×10^{5}	7.0×10^{3}	2.8×10^{5}	5.4×10^{3}	2.8×10^{5}	6.4×10^{3}
$k_{T_2\to S_1}$	500	3.3×10^{9}		1.3×10^{11}		9.4×10^{9}		
	400	4.0×10^{9}		1.4×10^{11}		9.9×10^{9}		
	350	4.6×10^{9}		1.5×10^{11}		1.0×10^{10}		
	298	5.5×10^{9}		1.6×10^{11}		1.0×10^{10}		

Table 3 shows both the calculated and experimentally measured ISC and RISC rates for S_1–T_1 and S_1–T_2 crossings. For S_1–T_1 crossings, the calculated ISC rates are in the same order of magnitude at three different temperatures (50, 100, and 298 K), indicating that the temperature effect on this ISC process is not so evident in the range of 50–298 K. On the other hand, the HT effect increases the ISC rate by more than one order of magnitude. For instance, at T=298 K and without VG approximation, the FC- and HT-like contributions in

ISC rates are 3.4×10^7 and 5.4×10^8 s^{-1}, respectively. The calculated results with the VG approximation show the similar tendency. The deviations between the calculated values with and without VG approximation are small, indicating that there is no much large difference between the PESs of two concerned singlet and triplet states. Regardless of whether VG approximation is invoked or not, the contribution of HTVC is much larger than FC. It is thus no doubt that the experimental ISC rate originates predominately from the contribution of the vibronic coupling.

For the RISC of S_1–T_1 crossings, increasing temperature evidently facilitates the corresponding rates. For example, as shown in Table 3, the calculated RISC rate at FC approximation increases from 1.9×10^4 to 3.1×10^5 s^{-1}. The HT contribution to the RISC rate is also one-order of magnitude larger than FC in room temperature. However, as the temperature increases, the difference between FC and HT contributions decreases.

Besides, Table 3 demonstrates that the theoretical calculations produce much larger ISC and RISC rate coefficients for S_1–T_2 crossings than those for S_1–T_1 crossings. This is reasonable because the former possess a much smaller energy gap and larger SOCME, shown in Tables 1 and 2. Considering the NAC vector between T_1–T_2 in Table 2, we deduce that the population transfer between singlet and triplet states of 7-PhQAD additionally takes place via S_1–T_2–T_1 channel except the direct S_1–T_1 transition.

The calculated rate coefficients by FC+HT approximation at room temperature are slightly larger than the experimentally-measured rates for both ISC and RISC processes. This deviation may originate from the neglecting of second-order SVC contribution, the inaccurate potential energy surfaces provided by TDDFT with TDA, and the improper description of complex experimental environment in our calculations. In our theoretical calculations, we assume a single molecule in the dilute solution and the solvent effect is accounted for by the PCM. The solute-solute and explicit solute-solvent intermolecular interactions, and the effect of environmental fluctuation are not taken into account, which would slow these transition processes down.

4.4 Rough estimation of SVC contribution to the crossing rates

To evaluate the impact of SVC effect among the low-lying excited states on the rates, we calculate the NAC vectors by the approaches[78–81] implemented within Q-Chem 5.2 package. As shown in Table 2, the calculated NAC vectors are relatively large. The NAC between T_1 and T_2 and between T_1 and T_3 even reach 19.50 and 7.79 au with respect to S_1 geometry, respectively. Meanwhile, we observe that the SOCMEs of T_2–S_1 and T_3–S_1 are much larger than that of T_1–S_1. Hence, the SVCs between the low-lying excited states definitely affect the ISC/RISC rates.

In above quantitative calculations of S–T crossing rates, we only include FC and HTVC contributions, a similar way as in Refs. 13 and 82, namely, only the first two terms of SOCME in Eq. (7) are involved. It is well known that $\frac{\partial H_{SO}^{fi}}{\partial Q_k}$ can be approximately written as

$$\begin{aligned}\frac{\partial H_{SO}^{fi}}{\partial Q_k} &= \langle^{\sigma'}\Psi_f|\frac{\hat{H}_{SO}}{\partial Q_k}|^{\sigma}\Psi_i\rangle \\ &+\sum_{m\neq i}\frac{H_{SO}^{fm}\langle^{\sigma}\Psi_m|\frac{\hat{H}^{el}}{\partial Q_k}|^{\sigma}\Psi_i\rangle}{E_i-E_m}+\sum_{n\neq f}\frac{\langle^{\sigma'}\Psi_n|\frac{\hat{H}^{el}}{\partial Q_k}|^{\sigma'}\Psi_f\rangle H_{SO}^{ni}}{E_f-E_n},\end{aligned} \tag{12}$$

based on the perturbed wavefunctions of the initial and final states. Here $\hat{H}^{el}$ is the electronic Hamiltonian, and $\langle^{\sigma}\Psi_e|\partial\hat{H}^{el}/\partial Q_k|^{\sigma}\Psi_r\rangle \approx (E_r - E_e)H_{er,\sigma}^{k}$. Therefore, the HT-type vibronically induced term provides mixing of the triplet and singlet excited-states, coupled with the first order vibronic perturbation due to the nuclear displacement along with the $3N-6$ normal modes Q. However, in this work, we account for the HTVC effect via directly evaluating the nuclear derivatives of SOC but not via calculating NAC vectors between the excited states. Considering large energy difference between S_1 and S_n, and the small value of $\langle^{\sigma'}\Psi_f|\frac{\hat{H}_{SO}}{\partial Q_k}|^{\sigma}\Psi_i\rangle$, the second term in RHS of Eq. (7) can be approximately written as

$$H'_{HT} \approx \sum_{k=1}^{3N-6}\sum_{n\neq f(i)} H_{nf(i),3}^{k}H_{SO}^{ni(f)}\langle\Lambda_f(Q')|Q_k|\Lambda_i(Q)\rangle, \tag{13}$$

and the last two terms in RHS of Eq. (7) become

$$H'_{SVC} \approx -\sum_{k=1}^{3N-6} \sum_{n \neq f(i)} \frac{H^k_{nf(i),3} H^{ni(f)}_{SO}}{E_{f(i)} - E_n} \langle \Lambda_f(Q') | \frac{\partial}{\partial Q_k} | \Lambda_i(Q) \rangle. \tag{14}$$

It is noted that the contribution from the intermediate singlet states $S_n (n > 1)$ is neglected.

Compared to the contribution of HTVC to the rate, the contribution of SVC will additionally be affected by the energy difference of $E_{T_1} - E_{T_n}$. In Section S3 of SI, we show the nuclear derivatives of SOCME between S_1 and T_1, and the value of $-\sum_{n=2,3} \frac{H^k_{T_n T_1} H^{S_1 T_n}_{SO}}{E_{T_1} - E_{T_n}}$. The latter is three orders of magnitude larger than the former. Associating with the vibrational function factors, we estimate that the contribution of SVC to the ISC and RISC rates will roughly be one order of magnitude larger than that of HTVC. We thus deduce that the SVC effect on the ISC and RISC rates of 7-PhQAD is predominant, agreeing with the previous prediction on the other MR-type TADF emitters.[25,29]

5 Conclusion

We have performed a theoretical study on the electronic structures, the photophysical properties, and the rate coefficients of the S–T crossings for 7-PhQAD molecule, a newly synthesized MR-type TADF emitter. We found that the HTVC effect on the absorption and fluorescence spectra is negligibly small while it plays a crucial role in the rate coefficients of S–T crossings. The HTVC effect increases the ISC rate by more than one order of magnitude.

Due to the small energy differences between the low-lying triplet states and larger SOCMEs between S_1 and $T_n (n = 2, 3)$ than that between S_1 and T_1, the contribution of SVC effect to the rates of S_1–T_1 crossings is roughly one order of magnitude larger than that of HTVC effect. For example, at ADC(2) level, the excitation energy differences between T_2 (T_3) and T_1 are only 0.22 (0.33) eV, and S_1 and T_2 states are nearly degenerate. It is well known that there is a strong vibrational coupling between two nearly degenerate excited electronic

states. Therefore, the experimentally measured ISC rate of 7-PhQAD originates predominantly from the vibronic coupling effects, and the NACs between the low-lying triplet excited states play a key role. It is insufficient to reproduce such a fast experimental ISC rate if only the direct SOC between the first singlet and triplet state is incorporated because of the larger energy gap of 0.19 eV and the small SOCME of 0.14 cm^{-1}. At T=298 K, FC approximation produces a ISC/RISC rate for S_1–T_2 crossing which is four orders of magnitude larger than that for S_1–T_1 crossing. Considering the contribution of SVC to the rates, we conclude that the vibronic coupling significantly enhances the population transfer via the channel of S_1–T_2–T_1.

However, there exists obvious deviation between the calculated and experimental rates, attributed to the inaccurate excited-state PESs produced by TDA and improperly accounting for the complex experimental situation. Like many other MR-type TADF emitters, 7-PhQAD holds a strongly electron correlation. Though its low-lying excited states are single excitation dominated states, more than 10% second-order dynamic correlation shown by ADC(2) calculated results suggests that the more sophisticated quantum chemistry methods should be used to exactly describe its excited states. The TDDFT method not only overestimates ΔE_{ST} but also the difference of the PESs between S_1 and S_0 states. The latter results in the significant enhancement of the vibrational motion, leading to the broadband absorption and emission when the difference of PESs between S_1 and S_0 states is taken into account. The calculation with VG approximation can successfully reproduce the experimental spectral lineshape. Additionally, in this theoretical calculation, a single molecule is assumed to be embedded by the dielectric continuum media, so that the solute-solute and explicit solute-solvent interactions and the environmental fluctuation are neglected, leading to the overestimated rate coefficients.

This work demonstrates a way to quantitatively predict the ISC and RISC rates of TADF emitters with including the vibronic coupling effect. Our calculations unveil the dynamical mechanism for highly efficient OLED emission and open design routes that go beyond the

FC approximation for the future development of high-performance devices.

Acknowledgement

Financial support from the National Natural Science Foundation of China (Grant Nos. 21833006, 22173074 and 21973043) is gratefully acknowledged. HM thank the financial support from the Hefei National Laboratory for Physical Sciences at the Microscale with grant No. KF2020103.

Supporting Information Available

The supplementary materials include the derivation about the FC- and HT-related terms and the damping-related term in the time-dependent approach; the rough evaluation of the SVC contribution to the rates, the excitation energies of 7-PhQAD calculated by ADC(2)/cc-pVDZ at the S_0 and S_1 geometries; the main geometrical parameters for the ground and excited-state geometries of 7-PhQAD; the selected molecular orbitals and the relaxed difference densities between the corresponding excited states and ground state by CAM-B3LYP*; and the differences between the optimized geometry of S_0, S_1, and T_1 states at TD-CAM-B3LYP*/6-311++G** level in toluene.

References

(1) Tang, C. W.; Vanslyke, S. A. Organic Electroluminescent Diodes. *Appl. Phys. Lett.* **1987**, *51*, 913–915.

(2) Adachi, C.; Baldo, M. A.; Thompson, M. E.; Forrest, S. R. Nearly 100% Internal Phosphorescence Efficiency in an Organic Light-Emitting Device. *J. Appl. Phys.* **2001**, *90*, 5048–5051.

(3) Uoyama, H.; Goushi, K.; Shizu, K.; Nomura, H.; Adachi, C. Highly Efficient Organic Light-Emitting Diodes from Delayed Fluorescence. *Nature* **2012**, *492*, 234–238.

(4) Godumala, M.; Choi, S.; Cho, M. J.; Choi, D. H. Recent Breakthrough in Thermally Activated Delayed Fluorescence Organic Light Emitting Diodes Containing Non-doped Emitting Layer. *J. Mater. Chem. C* **2019**, *7*, 2172–2198.

(5) Kondo, Y.; Yoshiura, K.; Kitera, S.; Nishi, H.; Hatakeyama, T. Narrowband Deep-Blue Organic Light-Emitting Diode Featuring an Organoboron-Based Emitter. *Nat. Photonics.* **2019**, *13*, 678–682.

(6) Segal, M.; Baldo, M. A.; Holmes, R. J.; Forrest, S. R.; Soos, Z. G. Excitonic Singlet-Triplet Ratios in Molecular and Polymeric Organic Materials. *Phys. Rev. B* **2003**, *68*, 75211.

(7) Godumala, M.; Choi, S.; Cho, M. J.; Choi, D. H. Thermally Activated Delayed Fluorescence Blue Dopants and Hosts: From the Design Strategy to Organic Light-Emitting Diode Applications. *J. Mater. Chem. C* **2016**, *4*, 11355–11381.

(8) Ogawa, S. *Organic Electronics Materials and Devices*; Springer: Tokyo, 2015.

(9) Hatakeyama, T.; Shiren, K.; Nakajima, K. Ultrapure Blue Thermally Activated Delayed Fluorescence Molecules: Efficient HOMO–LUMO Separation by the Multiple Resonance Effect. *Adv. Mater.* **2016**, *28*, 2777–2781.

(10) Shuai, Z. G.; Peng, Q. Excited States Structure and Processes: Understanding Organic Light-Emitting Diodes at the Molecular Level. *Phys. Rep.* **2014**, *537*, 123–156.

(11) Shuai, Z. G.; Peng, Q. Organic Light-Emitting Diodes: Theoretical Understanding of Highly Efficient Materials and Development of Computational Methodology. *Natl. Sci. Rev.* **2017**, *4*, 224–239.

(12) Baryshnikov, G.; Minaev, B.; Ågren, H. Theory and Calculation of the Phosphorescence Phenomenon. *Chem. Rev.* **2017**, *117*, 6500–6537.

(13) Marian, C. M. Spin-Orbit Coupling Intersystem Crossing in Molecules. *WIREs Comput. Mol. Sci.* **2012**, *2*, 187–203.

(14) Albrecht, A. C. Vibronic Spin-Orbit Perturbations and the Assignment of the Lowest Triplet State of Benzene. *J. Chem. Phys.* **1963**, *38*, 354–365.

(15) Lim, E. C.; Yu, J. M. H. Vibronic Spin-Orbit Interactions in Heteroaromatic Molecules. II. Phosphorescence of Quinoxaline and Other Diazanaphthalenes. *J. Chem. Phys.* **1968**, *49*, 3878–3884.

(16) Henry, B. R.; Siebrand, W. Spin-Orbit Coupling in Aromatic Hydrocarbons. Analysis of Nonradiative Transitions between Singlet and Triplet States in Benzene and Naphthalene. *J. Chem. Phys.* **1971**, *54*, 1072–1085.

(17) Tatchen, J.; Gilka, N.; Marian, C. M. Intersystem Crossing Driven by Vibronic Spin-Orbit Coupling: A Case Study on Psoralen. *Phys. Chem. Chem. Phys.* **2007**, *9*, 5209–5221.

(18) Etinski, M.; Tatchen, J.; Marian, C. M. Time-Dependent Approaches for the Calculation of Intersystem Crossing Rates. *J. Chem. Phys.* **2011**, *134*, 154105.

(19) Etinski, M.; Rai-Constapel, V.; Marian, C. M. Time-Dependent Approach to Spin-Vibronic Coupling: Implementation and Assessment. *J. Chem. Phys.* **2014**, *140*, 114104.

(20) Peng, Q.; Niu, Y.; Shi, Q.; Gao, X.; Shuai, Z. G. Correlation Function Formalism for Triplet Excited State Decay: Combined Spin-Orbit and Nonadiabatic Couplings. *J. Chem. Theory Comput.* **2013**, *9*, 1132–1143.

(21) Gibson, J.; Monkman, A. P.; Penfold, T. J. The Importance of Vibronic Coupling for Efficient Reverse Intersystem Crossing in Thermally Activated Delayed Fluorescence Molecules. *ChemPhysChem* **2016**, *17*, 2956–2961.

(22) Penfold, J. T.; Gindensperger, E.; Daniel, C.; Marian, C. M. Spin-Vibronic Mechanism for Intersystem Crossing. *Chem. Rev.* **2018**, *118*, 6975–7025.

(23) Föller, J.; Marian, C. M. Rotationally Assisted Spin-State Inversion in Carbene-Metal-Amides Is an Artifact. *J. Phys. Chem. Lett.* **2017**, *8*, 5643–5647.

(24) Ou, Q.; Peng, Q.; Shuai, Z. G. Toward Quantitative Prediction of Fluorescence Quantum Efficiency Through Combining Direct Vibrational Conversion and Surface Crossing: BODIPYs as Example. *J. Phys. Chem. Lett.* **2020**, *11*, 7790–7797.

(25) Kim, I.; Jeon, S. O.; Jeong, D.; Choi, H.; Lee, H. S. Spin-Vibronic Model for Quantitative Prediction of Reverse Intersystem Crossing Rate in Thermally Activated Delayed Fluorescence Systems. *J. Chem. Theory Comput.* **2020**, *16*, 621–632.

(26) Peng, Q.; Fan, D.; Duan, R.; Yi, Y.; Niu, Y.; Wang, D.; Shuai, Z. G. Theoretical Study of Conversion and Decay Processes of Excited Triplet and Singlet States in a Thermally Activated Delayed Fluorescence Molecule. *J. Phys. Chem. C* **2017**, *121*, 13448–13456.

(27) Chen, X.-K.; Zhang, S.-F.; Fan, J.-X.; Ren, A.-M. Nature of Highly Efficient Thermally Activated Delayed Fluorescence in Organic Light-Emitting Diode Emitters: Nonadiabatic Effect between Excited States. *J. Phys. Chem. C* **2015**, 119, 9728.

(28) Northey, T.; Penfold, T. J. The Intersystem Crossing Mechanism of An Ultrapure Blue Organoboron Emitter. *Org. Electron.* **2018**, 59, 45–48.

(29) Kim, I.; Cho, K. H.; Jeon, S. O.; Son, W. J.; Kim, D.; Rhee, Y. M.; Jang, I.; Choi, H.; Kim, D. S. Three States Involving Vibronic Resonance is a Key to Enhancing Re-

verse Intersystem Crossing Dynamics of an Organoboron-Based Ultrapure Blue Emitter. *JACS Au* **2021**, 1, 987–997.

(30) Patil, V. V.; Lee, H. L.; Kim, I.; Lee, K. H.; Chung, W. J.; Kim, J.; Park, S.; Choi, H.; Son, W.; Jeon, S. O; Lee, J. Y. Purely Spin-Vibronic Coupling Assisted Triplet to Singlet Up-Conversion for Real Deep Blue Organic Light-Emitting Diodes with Over 20% Efficiency and y Color Coordinate of 0.05. *Adv. Sci.* **2021**, 8, 2101137.

(31) Herzberg, G. *Electronic Spectra and Electronic Structure of Polyatomic Molecules*; Van Nostrand: Princeton, NJ, 1967.

(32) Mchale, J. L. *Molecular spectroscopy*; Pearson College Div: New Haven, Connecticut, USA, 1998.

(33) Santoro, F.; Lami, A.; Improta, R.; Bloino, J.; Barone, V. Effective Method for the Computation of Optical Spectra of Large Molecules at Finite Temperature Including the Duschinsky and Herzberg-Teller Effect: The Qx Band of Porphyrin as a Case Study. *J. Chem. Phys.* **2008**, *128*, 1724.

(34) Barone, V. *Computational Strategies for Spectroscopy. From Small Molecules to Nano Systems*; Wiley, Ltd.: Chichester, United Kingdom, 2011.

(35) Spiro, T. G.; Stein, P. Resonance Effects in Vibrational Scattering From Complex Molecules. *Annu. Rev. Phys. Chem.* **1977**, *28*, 501–521.

(36) Myers, A. B. Resonance Raman Intensities and Charge-Transfer Reorganization Energies. *Chem. Rev.* **1996**, *96*, 911–926.

(37) Myers, A. B. Resonance Raman Intensity Analysis of Excited-State Dynamics. *Acc. Chem. Res.* **1997**, *30*, 519–527.

(38) Ma, H. L.; Liu, J.; Liang, W. Z. Time-Dependent Approach to Resonance Raman

Spectra Including Duschinsky Rotation and Herzberg-Teller Effects: Formalism and Its Realistic Applications. *J. Chem. Theory Comput.* **2012**, *8*, 4474–4482.

(39) Liang, W. Z.; Zhao, Y.; Sun, J.; Song, J.; Yang, J. L. Electronic Excitation of Polyfluorenes: A Theoretical Study. *J. Phys. Chem. B* **2006**, *110*, 9908–9915.

(40) Ma, H. L.; Zhao, Y.; Liang, W. Z. Assessment of Mode-Mixing and Herzberg-Teller Effects on Two-Photon Absorption and Resonance Hyper-Raman Spectra from a Time-Dependent Approach. *J. Chem. Phys.* **2014**, *140*, 94107.

(41) Liang, W. Z.; Ma, H. L.; Zang, H.; Ye, C. X. Generalized Time-Dependent Approaches to Vibrationally Resolved Electronic and Raman Spectra: Theory and Applications. *Int. J. Quantum Chem.* **2015**, *115*, 550–563.

(42) Duschinsky, F. On the Interpretation of Electronic Spectra of Polyatomic Molecules I: The Franck-Condon principle. *Acta. Phys-Chim. URSS* **1937**, *7*, 551.

(43) Ferrer, F. J. A.; Barone, V.; Cappelli, C.; Santoro, F. Duschinsky, Herzberg-Teller, and Multiple Electronic Resonance Interferential Effects in Resonance Raman Spectra and Excitation Profiles. The Case of Pyrene. *J. Chem. Theory Comput.* **2013**, *9*, 3597–3611.

(44) Li, X.; Shi, Y.-Z.; Wang, K.; Zhang, M.; Zheng, C.-J.; Sun, D.-M.; Dai, G.-L.; Fan, X.-C.; Wang, D.-Q.; Liu, W.; Li, Y.-Q.; Yu, J.; Ou, X.-M.; Adachi, C.; Zhang, X.-H. Thermally Activated Delayed Fluorescence Carbonyl Derivatives for Organic Light-Emitting Diodes with Extremely Narrow Full Width at Half-Maximum. *ACS Appl. Mater. Interfaces* **2019**, *11*, 13472–13480.

(45) El-sayed, M. A. Spin-Orbit Coupling and the Radiationless Processes in Nitrogen Heterocyclics. *J. Chem. Phys.* **1963**, *38*, 2834–2838.

(46) Feshbach, H. *Quantum Mechanics.*; American Association for the Advancement of Science: Nwe York, 1962.

(47) Lawetz, V.; Orlandi, G.; Siebrand, W. Theory of Intersystem Crossing in Aromatic Hydrocarbons. *J. Chem. Phys.* **1972**, *56*, 4058–4072.

(48) Mukamel, S. *The Principles of Nonlinear Optical Spectroscopy*; Oxford University Press: New York, 1995.

(49) Zhao, Y.; Liang, W. Z. Charge Transfer in Organic Molecules for Solar Cells: Theoretical Perspective. *Chem. Soc. Rev.* **2012** *41*, 1075–1087.

(50) Hirata, S.; Sakai, Y.; Masui, K.; Tanaka, H.; Lee, S. Y.; Nomura, H.; Nakamura, N.; Yasumatsu, M.; Nakanotani, H.; Zhang, Q.; Shizu, K.; Miyazaki, H.; Adachi, C. Highly Efficient Blue Electroluminescence Based on Thermally Activated Delayed Fluorescence. *Nat. Mater.* **2014**, *14*, 330–336.

(51) Dias, F. B.; Penfold, T. J.; Monkman, A. P. Photophysics of Thermally Activated Delayed Fluorescence Molecules. *Methods Appl. Fluoresc.* **2017**, *5*, 012001.

(52) Wong, M. Y.; Zysman-Colman, E. Purely Organic Thermally Activated Delayed Fluorescence Materials for Organic Light-Emitting Diodes. *Adv. Mater.* **2017**, *29*, 1605444.

(53) Penfold, T. J.; Dias, F. B.; Monkman, A. P. The Theory of Thermally Activated Delayed Fluorescence for Organic Light Emitting Diodes. *Chem. Commun.* **2018**, *54*, 3926–3935.

(54) Yersin, H. *Highly Efficient OLEDs with Phosphorescent Materials*; Wiley-VCH: Weinheim, 2008.

(55) Körzdörfer, T.; Sears, J. S.; Sutton, C.; Brédas, J.-L. Long-Range Corrected Hybrid Functionals for π-Conjugated Systems: Dependence of the Range-Separation Parameter on Conjugation Length. *J. Chem. Phys.* **2011**, *135*, 204107.

(56) Sun, H. T.; Zhong, C.; Sun, Z. R. Recent Advances in the Optimally "Tuned" Range-Separated Density Functional Theory. *Acta. Phys-Chim. Sin.* **2016**, *32*, 2197–2208.

(57) Stein, T.; Kronik, L.; Baer, R. Reliable Prediction of Charge Transfer Excitations in Molecular Complexes Using Time-Dependent Density Functional Theory. *J. Am. Chem. Soc.* **2009**, *131*, 2818–2820.

(58) Tu, C. Y.; Liang, W. Z. NB-Type Electronic Asymmetric Compounds as Potential Blue-Color TADF Emitters: Steric Hindrance, Substitution Effect, and Electronic Characteristics. *ACS Omega* **2017**, *2*, 3098–3109.

(59) Tu, C. Y.; Liang, W. Z. Benzazasiline Combined with Triphenylborane-Based Cores for Constructing Deep-Blue Donor-Acceptor-Donor TADF Emitters. *Org. Electron.* **2018**, *57*, 74–81.

(60) Stephens, P. J.; Devlin, F. J.; Chabalowski, C. F.; Frisch, M. J. Ab Initio Calculation of Vibrational Absorption and Circular Dichroism Spectra Using Density Functional Force Fields. *J. Phys. Chem.* **1994**, *98*, 11623–11627.

(61) Yanai, T.; Tew, D. P.; Handy, N. C. A New Hybrid Exchange-Correlation Functional Using the Coulomb-Attenuating Method (CAM-B3LYP). *Chem. Phys. Lett.* **2004**, *393*, 51–57.

(62) Leininger, T.; Stoll, H.; Werner, H. J.; Savin, A. Combining Long-Range Configuration Interaction with Short-Range Density Functionals. *Chem. Phys. Lett.* **1997**, *275*, 151–160.

(63) Chai, J. D.; Head-Gordon, M. Long-Range Corrected Hybrid Density Functionals with Damped Atom-Atom Dispersion Corrections. *Phys. Chem. Chem. Phys.* **2008**, *10*, 6615–6620.

(64) Ai, W.; Fang, W. H.; Su, N. Q. The Role of Range-Separated Correlation in Long-Range Corrected Hybrid Functionals. *J. Phys. Chem. Lett.* **2021**, *12*, 1207–1213.

(65) Kronik, L.; Stein, T.; Refaely-Abramson, S.; Baer, R. Excitation Gaps of Finite-Sized Systems from Optimally Tuned Range-Separated Hybrid Functionals. *J. Chem. Theory Comput.* **2012**, *8*, 1515–1531.

(66) Sun, H.; Zhong, C.; Brédas, J.-L. Reliable Prediction with Tuned Range-Separated Functionals of the Singlet-Triplet Gap in Organic Emitters for Thermally Activated Delayed Fluorescence. *J. Chem. Theory Comput.* **2015**, *11*, 3851–3858.

(67) Miertuš, S.; Scrocco, E.; Tomasi, J. Electrostatic Interaction of a Solute with a Continuum. A Direct Utilizaion of AB Initio Molecular Potentials for the Prevision of Solvent Effects. *Chem. Phys.* **1981**, *55*, 117–129.

(68) Miertuš, S.; Tomasi, J. Approximate Evaluations of the Electrostatic Free Energy and Internal Energy Changes in Solution Processes. *Chem. Phys.* **1982**, *65*, 239–245.

(69) Cammi, R.; Mennucci, B.; Tomasi, J. Fast Evaluation of Geometries and Properties of Excited Molecules in Solution: A Tamm-Dancoff Model with Application to 4-Dimethylaminobenzonitrile. *J. Phys. Chem. A* **2000**, *104*, 5631–5637.

(70) Epifanovsky, E.; Gilbert, A. T. B.; Feng, X.; Lee, J.; Mao, Y.; Mardirossian, N.; Pokhilko, P.; White, A. F.; Coons, M. P.; Dempwolff, A. L.; et al. Software for The Frontiers of Quantum Chemistry: An Overview of Developments in the Q-Chem 5 Package. *J. Chem. Phys.* **2021**, *155*, 084801.

(71) Hirata, S.; Head-Gordon, M. Time-dependent Density Functional Theory Within the Tamm-Dancoff Approximation. *Chem. Phys. Lett.* **1999**, *314*, 291–299.

(72) Wenzel, J.; Wormit, M.; and Dreuw. A. Calculating X-ray Absorption Spectra of Open-Shell Molecules with the Unrestricted Algebraic-Diagrammatic Construction Scheme for the Polarization Propagator. *J. Chem. Theory Comput.* **2014**, *10*, 4583-4598.

(73) Lu, T.; Chen, F. W. Multiwfn: A Multifunctional Wavefunction Analyzer. *J. Comput. Chem.* **2012**, *33*, 580–592.

(74) Liu, Z. Y.; Lu, T.; Chen, Q. X. An Sp-Hybridized All-Carboatomic Ring, Cyclo[18]Carbon: Electronic Structure, Electronic Spectrum, and Optical Nonlinearity. *Carbon* **2020**, *165*, 461–467.

(75) de Silva, P. Inverted Singlet–Triplet Gaps and Their Relevance to Thermally Activated Delayed Fluorescence. *J. Phys. Chem. Lett.*, **2019**, 10, 5674–5679.

(76) Pershin, A.; Hall, D.; Lemaur, V.; Sancho-Garcia, J.-C.; Muccioli, L.; Zysman-Colman, E.; Beljonne, D. Olivier, Y. Highly emissive excitons with reduced exchange energy in thermally activated delayed fluorescent molecules *Nat. Commun.*, **2019**, 10, 597.

(77) Santoro, F.; Cappelli, C.; Barone, V. Effective Time-Independent Calculations of Vibrational Resonance Raman Spectra of Isolated and Solvated Molecules Including Duschinsky and Herzberg-Teller Effects. *J. Chem. Theory Comput.* **2011**, *7*, 1824–1839.

(78) Fatehi, S.; Alguire, E.; Shao, Y. H.; Subotnik, J. E. Analytic Derivative Couplings between Configuration-Interaction-Singles States with Built-in Electron-Translation Factors for Translational Invariance. *J. Chem. Phys.* **2011**, *135*, 234105.

(79) Zhang, X.; Herbert, J. M. Analytic Derivative Couplings for Spin-Flip Configuration Interaction Singles and Spin-Flip Time-Dependent Density Functional Theory. *J. Chem. Phys.* **2014**, *141*, 64104.

(80) Ou, Q.; Bellchambers, G. D.; Furche, F.; Subotnik, J. E. First-Order Derivative Couplings between Excited States from Adiabatic TDDFT Response Theory. *J. Chem. Phys.* **2015**, *142*, 64114.

(81) Zhang, X.; Herbert, J. M. Analytic Derivative Couplings in Time-Dependent Den-

sity Functional Theory: Quadratic Response Theory Versus Pseudo-Wavefunction Approach. *J. Chem. Phys.* **2015**, *142*, 64109.

(82) Valiev, R. R.; Cherepanov, V. N.; Nasibullin, R. T.; Sundholm, D.; Kurten, T. Calculating rate constants for intersystem crossing and internal conversion in the Franck–Condon and Herzberg–Teller approximations. *Phys. Chem. Chem. Phys.* **2019**, *21*, 18495–18500.

TOC Graphic

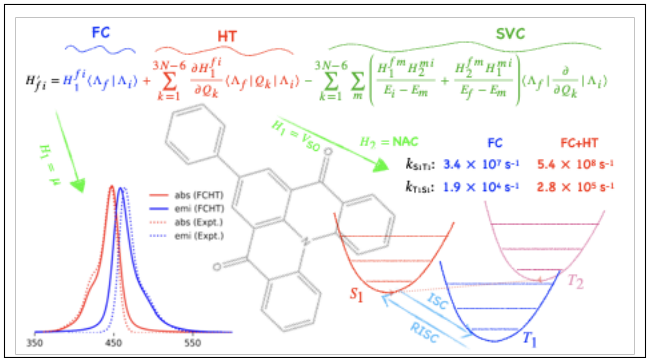
FC
HT
SVC
$H^{fi}_{fi} = H^{fi}_{1}\langle\Lambda_f|\Lambda_i\rangle + \sum_{k=1}^{3N-6}\frac{\partial H^{fi}_{1}}{\partial Q_k}\langle\Lambda_f|Q_k|\Lambda_i\rangle - \sum_{k=1}^{3N-6}\sum_{m}\left(\frac{H^{fm}_{1}H^{mi}_{2}}{E_i - E_m} + \frac{H^{fm}_{2}H^{mi}_{1}}{E_f - E_m}\right)\langle\Lambda_f|\frac{\partial}{\partial Q_k}|\Lambda_i\rangle$
$H_1 = \mu$
$H_1 = V_{SO}$
H_2 = NAC
FC
FC+HT
$k_{S_1T_1}$: 3.4 × 10^7 s^{-1} 5.4 × 10^8 s^{-1}
$k_{T_1S_1}$: 1.9 × 10^4 s^{-1} 2.8 × 10^5 s^{-1}
abs (FCHT)
emi (FCHT)
abs (Expt.)
emi (Expt.)
350
450
550
S_1
T_2
T_1
ISC
RISC